Computer Modeling in Engineering & Sciences

Tech Science Press

DOI: 10.32604/cmes.2022.020911

ARTICLE

Stability Scrutinization of Agrawal Axisymmetric Flow of Nanofluid through a Permeable Moving Disk Due to Renewable Solar Radiation with Smoluchowski Temperature and Maxwell Velocity Slip Boundary Conditions

Umair Khan[1,2], Aurang Zaib[3], Anuar Ishak[1], Iskandar Waini[4], El-Sayed M. Sherif[5] and Dumitru Baleanu[6,7,8,*]

[1]Department of Mathematical Sciences, Faculty of Science and Technology, Universiti Kebangsaan Malaysia, Bangi, 43600, Malaysia

[2]Department of Mathematics and Social Sciences, Sukkur IBA University, Sukkur, 65200, Pakistan

[3]Department of Mathematical Sciences, Federal Urdu University of Arts, Science & Technology, Karachi, 75300, Pakistan

[4]Fakulti Teknologi Kejuruteraan Mekanikal dan Pembuatan, Universiti Teknikal Malaysia Melaka, Melaka, 76100, Malaysia

[5]Mechanical Engineering Department, College of Engineering, King Saud University, Riyadh, 11423, Saudi Arabia

[6]Department of Mathematics, Cankaya University, Ankara, 06790, Turkey

[7]Institute of Space Sciences, Magurele, 077125, Romania

[8]Department of Medical Research, China Medical University Hospital, China Medical University, Taichung, 40447, Taiwan

*Corresponding Author: Dumitru Baleanu. Email: dumitru@cankaya.edu.tr

Received: 19 December 2021 Accepted: 13 April 2022

ABSTRACT

The utilization of solar energy is essential to all living things since the beginning of time. In addition to being a constant source of energy, solar energy (SE) can also be used to generate heat and electricity. Recent technology enables to convert the solar energy into electricity by using thermal solar heat. Solar energy is perhaps the most easily accessible and plentiful source of sustainable energy. Copper-based nanofluid has been considered as a method to improve solar collector performance by absorbing incoming solar energy directly. The goal of this research is to explore theoretically the Agrawal axisymmetric flow induced by Cu-water nanofluid over a moving permeable disk caused by solar energy. Moreover, the impacts of Maxwell velocity and Smoluchowski temperature slip are incorporated to discuss the fine points of nanofluid flow and characteristics of heat transfer. The primary partial differential equations are transformed to similarity equations by employing similarity variables and then utilizing bvp4c to resolve the set of equations numerically. The current numerical approach can produce double solutions by providing suitable initial guesses. In addition, the results revealed that the impact of solar collector efficiency enhances significantly due to nanoparticle volume fraction. The suction parameter delays the boundary layer separation. Moreover, stability analysis is performed and is found that the upper solution is stable and physically trustworthy while the lower one is unstable.

KEYWORDS

Agrawal axisymmetric flow; solar energy; nanofluid; heat transfer; slip conditions

Nomenclature

T_∞	Constant ambient temperature (K)
b	Constant parameter having units $(m.s)^{-1}$
(r_a, θ_a, z_a)	Cylindrical coordinate system (m)
T_w	Constant surface temperature (K)
w_A	Constant mass flux velocity (m/s)
$G(\xi)$	Dimensionless velocity stream function
u_e, v_e, w_e	Free-stream velocities (m/s)
Nu_{ra}	Local Nusselt number
Re_{ra}	Local Reynolds number
P_a	Pressure $(kg/m.s^2)$
Pr	Prandtl number
N_r	Radiation parameter
q_r	Radiative heat flux
u_w	Surface velocity of the disk (m/s)
f_w	Suction parameter
C_{fra}	Skin friction coefficient along the radial direction
c_p	Specific heat at constant pressure (J/kg.K)
k	Thermal conductivity (W/(m. K))
T_a	Temperature of the fluid (K)
(u_a, v_a, w_a)	Velocity components (m/s)

Greek symbols

μ	Absolute viscosity $(N.s/m^2)$
λ_a	Coefficient of the main free path
ρ	Density (kg/m^3)
$S(\xi)$	Dimensionless temperature
Γ	Eigenvalue
υ_f	Kinematic viscosity (m^2/s)
k^a	Mean absorption constant
Σ	New dimensionless variable
ξ	Pseudo-similarity variable
β_A	Stretching/Shrinking parameter
γ_A	Specific heat ratio
σ^a	Stefan-Boltzmann constant $(W/(m^2.K^4))$
φ	Solid nanoparticle volume fraction
σ_{TA}	Thermal accommodation coefficient
α_f	Thermal diffusivity (m^2/s)
δ_B	Temperature slip parameter
σ_w	Tangential momentum accommodation coefficient
δ_A	Velocity slip parameter

Acronyms

bvp4c	Boundary value problem of the fourth-order
BCs	Boundary conditions

Cu	Copper
HS	Human society
ICs	Initial conditions
LBS	Lower branch solution
ODEs	Ordinary differential equations
PDEs	Partial differential equations
SE	Solar energy
SPF	Stagnation point flow
2D, 3D	Two and three-dimensional
UBS	Upper branch solution
H_2O	Water

Subscripts

∞	Far-field condition
nf	Nanofluid
s	Solid nanoparticles
f	Working base fluid
w	Wall boundary condition

Superscript

'	Derivative with respect to ξ

1 Introduction

Energy is critical to the advancement of human civilization or society (HS). Though, over the last century, the rapid advancement of HS has led to worldwide energy crises and severe environmental pollution. To find a way to sustainable development, all countries need to take advantage of new energy sources and develop new energy technologies. The sun is perhaps most likely the greatest clean source of heat in the form of energy accessible these days. Renewable sources of energy involve solar energy (which comes from the sun and can be converted into heat and electricity), hydropower from water, biomass from plants, geothermal energy (from within the earth), and wind energy. Solar energy, a renewable and environmentally approachable energy source, has been producing energy for thousands of years. Nanomaterials are new energy materials because their particle size is equal to or less than the wavelength of the coherent wave and the de Broglie wave. As a result, nanoparticles dissipate incident radiation both strongly and independently. The use of nanofluids in solar thermal systems has emerged as a new research focus predicated on the properties of radiative motion of nanoparticles. According to Angstrom [1] and Keshavarz et al. [2], SE is one of the best sources of renewable energy with the least amount of environmental impact. In the 1970s, Hunt [3] gave a basic idea of utilizing particles to capture solar energy. The situation has been demonstrated that merging nanomaterials in a liquid (nanofluid) has a significant impact on the liquid's thermophysical characteristics, like thermal conductivity. Lu et al. [4] utilized nanofluids in solar collectors through vacated tubes. Kandasamy et al. [5] utilized the Hiemenz time-dependent flow of Cu-water nanoparticles over a permeable wedge due to SE with thermal stratification and applied Lie group analysis to find the numerical solution. Anbuchezhian et al. [6] scrutinized the magneto liquid flow with heat transfer via a nanoparticle over a vertical porous stretchable sheet owing to solar radiation. They detected that the profiles of temperature enrich due to radiation impact. The time-dependent (TD) magneto flow conveying by

nanofluid past a permeable wedge in a non-Darcy porous medium was inspected by Kandasamy et al. [7]. They observed that the copper nanoparticles played an important role and absorb solar radiation incidents. Makinde et al. [8] discussed the impacts of Joule heating and chemical reaction on the magneto flow in a nanofluid through a heated stretchable sheet induced in a porous medium with solar radiation. The surface concentration and temperature gradients are found to be increasing functions of the non-Darcy parameter. Talebi et al. [9] experimentally inspected the forced convection flow and heat transfer induced by hybrid nanofluids with the fixed condition of heat flux in the laminar regime. Acharya [10] quantified the pattern of the flow and the behavior of heat transfer containing hybrid nanofluid induced by erratic solar radiation for different thermal apparatus of solar. Asadikia et al. [11,12] prepared high-performance nanofluids using the electrical and thermal conductivities of carbon nanotubes and copper oxide nanoparticles to improve the properties of heat transfer. According to the experimental data, the thermal conductivity increases proportionally to the number of nanoparticles but decreases in alkaline environments. Sarkar et al. [13] evaluated the features of fluid flow of time-dependent nanoliquid towards a stagnation point through a spinning sphere owing to Hall current and solar radiation. Asadikia et al. [14] experimentally scrutinized the water and ethylene glycol-based Fe_2O_3/SWCNT hybrid nanofluid by using genetic algorithms and neural networks. The entropy analysis of fluid flow within a slant permeable cavity induced by hybrid nanofluid with heat generation was examined by Chamkha et al. [15]. They observed that the dispersion of nanoparticles reduces thermal performance for several Rayleigh numbers. Recently, Shoeibi et al. [16] evaluated the performance of a solar still by employing hybrid nanofluids cooling of the glass. The temperature difference between condensation and evaporation areas is increased by hybrid nanofluid protection cooling.

The slip boundary condition is defined as the module of tangential speed at the body surface that is proportional to the wall gradients (shear stress). After establishing a link between slip rate and shear stress, Navier [17] coined the term slip boundary condition. Maxwell [18] gave the most basic enlightenment for the momentum slip, which is based on a momentum gradient accommodation exerting normal to the surface as well as the creep term. Later, Smoluchowski [19] goes on to illuminate the concept of slip temperature. Ramya et al. [20] inspected the impacts of momentum and thermal slips on the dynamics of fluid flow scattered in nanomaterials. The rates of heat and mass transfer are reduced as the thermal slip parameter is increased. Khashi et al. [21] elaborated the impressions of slip and CBCs on a 3D flow comprising two dissimilar kinds of nanomaterials over a stretching/shrinking surface. The stability analysis has been performed to validate the stable solution. Jünemann et al. [22] utilized the Smoluchowski temperature boundary as well as Maxwell slip condition to stimulate the behavior of operation of screw machines. Recently, Sajid et al. [23] developed a 3D model subject to Sutterby rotating fluid flow in an expandable slippery surface with Smoluchowski temperature and Maxwell slip conditions. They discovered that in the case of a constant reaction rate, the thermal radiation parameter improves the heat transfer by 17.2 percent and the mass transfer by 62.1 percent.

A rigid or stiff body moving via a fluid (i.e., automobile, sports ball, missile, space travel vehicle), or in the recovery of oil in the industry (the extraction of crude oil from a lubricant ground is accomplished through gas equivalently or injection), a stagnation point signifies as an exterior flow encroaches in a stationary-point on the exterior of a submerged body within a flow, where the speed of the object is zero at the surface of the submerged object. Hiemenz [24] was the first to precisely analyze the classic problem of 2D stagnation-point flows (SPFs). As a result, the flow guided perpendicular to a flat infinite plate has an exact solution. The axisymmetric flow (AF) near a stagnation point (SP) from a plate was investigated by Homann [25]. Ramya et al. [20] and Howarth [26] extended the 2D flow and axisymmetric flow to the 3D flow case using the approximation of the boundary layer in the

path normal to the plane surface. In addition, Davey [27] developed an innovative axisymmetric SPF and presented an analytic solution to the Navier–Stokes equations by using spherical coordinates. On the contrary to the Agrawal [28] outer irrotational flow, this flow is rotational in the far-field. Weidman [29] has prolonged Agrawal's work toward the situation of SP rotational flow impingement on a stretchable radially surface. Weidman [30,31] analyzed the AGAF near a SP from a respective stretched and flat sheet. Recently, Roşca et al. [32] investigated the viscous fluid flow impinging towards a stretching/shrinking sheet in a nanofluid and presented double solutions.

The axisymmetric flow past a permeable moving continuous disk in the existence of Maxwell and Smoluchowski slip conditions after being inspired by the literature mentioned aboveis simulated in this paper. In the existence of radiative solar energy, the thermal impartiality of the entire model is developed. The copper nanoparticles are used to simulate a flow with water as the base medium. There are very few publications dealing with axisymmetric flow induced by nanofluid flow past a stretching/shrinking sheet influenced by solar radiation. As a result, our novel exploration into the influence of radiative solar energy as well as slips interactions will help engineers implement nanofluids positively and effectively. The multiple solutions of the considered model are also one of the main interests of this work for the phenomena of shrinking and stretching disk. Therefore, stability analysis is also implemented to check which result is physically realizable.

2 Mathematical Modeling of the Problem

Consider the characteristics of heat transfer analysis and steady Agrawal axisymmetric SPF of a copper water-based nanofluid through a porous moving disk in the presence of solar energy radiation as shown schematically in Fig. 1. The flow configuration of the model is articulated in the form of cylindrical coordinates (r_a, θ_a, z_a) measured in the radial, azimuthal and axial directions respectively, along with accompanying velocity modules (u_a, v_a, w_a). The AGF is exclusively symmetric to the $r_a\theta_a-$plane and likewise axisymmetric to the coordinate z_a-axis, i.e., the change with respect to the coordinate θ_a is completely ignored. The surface is positioned at $z_a = 0$, and the upper half-plane is the essential domain of the fluid flow. Further presume that the variable far field or ambient velocity is emphasized via $u_e(r_a, z_a) = 2br_a z_a$ and $w_e(r_a, z_a) = -2bz_a^2$, where b corresponds the arbitrary factor evaluating the magnitude of the AGF having dimensions $(LT)^{-1}$, see Weidman [31]. In addition, the wall variable velocity is highlighted via $u_w = b^{2/3}\upsilon_f^{1/3} r_a$ along with the requisite posited Maxwell slip velocity [12] having slip length $\frac{2-\sigma_w}{\sigma_w}\lambda_a \frac{\partial u_a}{\partial z_a}$ have been employed to examine the momentum slip effect while the transparent constant mass flux is equal to w_A, where $w_A < 0$ is for the case of suction and $w_A > 0$ is for the case of blowing. The Smoluchowski temperature slip [19] and the wall constant temperature is designated via $\frac{2-\sigma_{TA}}{\sigma_{TA}}\left(\frac{2\gamma_A}{\gamma_A+1}\right)\frac{\lambda_a}{\mathrm{Pr}}\frac{\partial T_a}{\partial z_a}$ and T_w, respectively, while the free-stream constant temperature is denoted via T_∞ by means of the phenomenon $T_w > T_\infty$. The surroundings and the Newtonian absorber are both kept at a constant temperature T_∞, far away from the moving disk surface. Furthermore, an incoming radiation flux of intensity q_r is received by the non-reflective, absorbent, preferably transparent movable disk. Rendering to Fathalah et al. [33], this q_r penetrates the moving disk surface and is absorbed in a neighboring fluid with an absorption coefficient. Heat is transported from the disk surface to the surroundings as the absorbing nanoliquid and the moving disk surface are heated by SE. Also, solar radiation is a collimated beam that is perpendicular to the surface of the disk. As stated before, the regular (viscous) fluid is supposed to have heat absorption properties. However, the thermophysical properties of the working fluid and the nanoparticle are taken to be

constant. Due to the significant impression of the aforesaid assumptions of the problem, the leading constitutive equations in terms of PDEs can be simply and written as Eqs. (1)–(4) (see Weidman [31]):

$$\frac{1}{r_a}\frac{\partial\,(r_a u_a)}{\partial r_a}+\frac{\partial w_a}{\partial z_a}=0, \tag{1}$$

$$u_a\frac{\partial u_a}{\partial r_a}+w_a\frac{\partial u_a}{\partial z_a}=-\frac{1}{\rho_{nf}}\frac{\partial P_a}{\partial r_a}+\frac{\mu_{nf}}{\rho_{nf}}\left(\frac{\partial^2 u_a}{\partial r_a^2}-\frac{u_a}{r_a^2}+\frac{1}{r_a}\frac{\partial u_a}{\partial r_a}+\frac{\partial^2 u_a}{\partial z_a^2}\right), \tag{2}$$

$$u_a\frac{\partial w_a}{\partial r_a}+w_a\frac{\partial w_a}{\partial z_a}=-\frac{1}{\rho_{nf}}\frac{\partial P_a}{\partial z_a}+\frac{\mu_{nf}}{\rho_{nf}}\left(\frac{\partial^2 w_a}{\partial r_a^2}+\frac{1}{r_a}\frac{\partial w_a}{\partial r_a}+\frac{\partial^2 w_a}{\partial z_a^2}\right), \tag{3}$$

$$u_a\frac{\partial T_a}{\partial r_a}+w_a\frac{\partial T_a}{\partial z_a}=\frac{k_{nf}}{(\rho c_p)_{nf}}\left(\frac{\partial^2 T_a}{\partial r_a^2}+\frac{1}{r_a}\frac{\partial T_a}{\partial r_a}+\frac{\partial^2 T_a}{\partial z_a^2}\right)-\frac{1}{(\rho c_p)_{nf}}\frac{\partial q_r}{\partial z_a}, \tag{4}$$

along with subject to the boundary conditions in Eq. (5)

$$\left.\begin{aligned} &u_a=\beta_A u_w+\frac{2-\sigma_w}{\sigma_w}\lambda_a\frac{\partial u_a}{\partial z_a},\ w_a=w_A,\ T_a=T_w+\frac{2-\sigma_{TA}}{\sigma_{TA}}\left(\frac{2\gamma_A}{\gamma_A+1}\right)\frac{\lambda_a}{\mathrm{Pr}}\frac{\partial T_a}{\partial z_a}\ \text{at}\ z_a=0,\\ &\frac{\partial u_a}{\partial z_a}\to\frac{\partial u_e}{\partial z_a},\ T_a\to T_\infty\ \text{as}\ z_a\to\infty. \end{aligned}\right\} \tag{5}$$

Here, w_a and u_a are the velocity components along z_a and r_a axes, σ_w corresponds the coefficient of tangential momentum accommodation, P_a is the pressure, σ_{TA} corresponds the coefficient of thermal accommodation, λ_a corresponds the main free path coefficient, T_a corresponds the temperature, γ_A corresponds the specific heat ratio coefficient and β_A corresponds the dimensionless shrinking/stretching constraint with $\beta_A<0$ for shrinking, $\beta_A>0$ for stretching, and $\beta_A=0$ for the motionless disk.

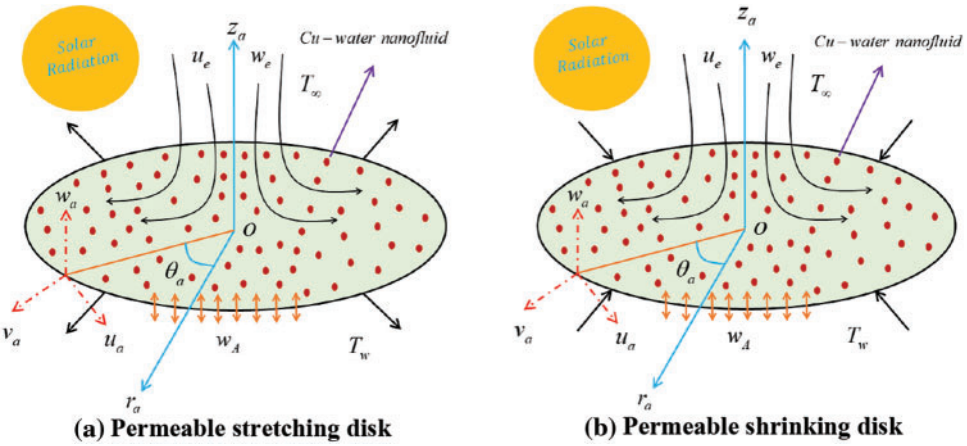

Figure 1: Physical model of the Agrawal flow problem

In addition, the thermo-physical expressions of the copper-water based nanofluid are set by [34] in Eq. (6):

$$\begin{cases} \dfrac{\mu_{nf}}{\mu_f} = (1-\varphi)^{-2.5}, \\ \dfrac{\rho_{nf}}{\rho_f} = \varphi\left(\dfrac{\rho_s}{\rho_f}\right) + (1-\varphi), \\ \dfrac{k_{nf}}{k_f} = \dfrac{(k_s+2k_f) - 2\varphi(k_f-k_s)}{(k_s+2k_f) + \varphi(k_f-k_s)}, \\ \dfrac{(\rho c_p)_{nf}}{(\rho c_p)_f} = \varphi\left(\dfrac{(\rho c_p)_s}{(\rho c_p)_f}\right) + (1-\varphi), \end{cases} \tag{6}$$

where φ namely resembles to the nanoparticles volume fraction which is equal to the mixtures of copper nanoparticle (Cu) and the regular (viscous) fluid (H_2O). Additionally, k_f, ρ_f, μ_f and $(\rho c_p)_f$ indicate the thermal conductivity, density, dynamic viscosity, and the specific heat capacity at a constant pressure of the regular (viscous) fluid, respectively, while k_s, ρ_s and $(\rho c_p)_s$ are the respective quantities of the solid nanoparticles. Moreover, the subscripts s and f are classified as the solid nanoparticles and the base fluid, respectively. The experimental thermophysical characteristics of the regular pure liquid (water) and copper (Cu) nanoparticles are depicted in Table 1.

Table 1: The thermophysical properties of Cu/water nanoparticles

Physical properties	Water	Cu
$k\,(W/m.K)$	0.613	400
$c_p\,(J/kg.K)$	4179	385
$\rho\,(kg/m^3)$	997.1	8933
Pr	6.2	–

Furthermore, the last term on the right-hand side of Eq. (4) is incorporated specially to demarcate the radiative heat flux q_r. Also, given an optically thick fluid (nanofluid) layer, one can express the simplified version of the q_r using the Rosseland approximation can be as Eq. (7) (see Hayat et al. [35]):

$$q_r = -\frac{4\sigma^a}{3k^a}\frac{\partial T_a^4}{\partial z_a}, \tag{7}$$

where σ^a and k^a signify the Stefan Boltzmann and the mean absorption constants. Using Taylor series approximation centered around the point T_∞, the term T_a^4 can be simplified as $T_a^4 \cong 4T_\infty^3 T_a - 3T_\infty^4$, by neglecting the second and higher order power terms.

For making the system of equations dimensionless, the following similarity variables are employed in Eq. (8) (see Weidman [31]):

$$\begin{aligned} &u_a(r_a, z_a) = b^{2/3}\upsilon_f^{1/3} r_a G'(\xi), \xi = (b/\upsilon_f)^{1/3} z_a, S(\xi) = \frac{T_a - T_\infty}{T_w - T_\infty}, \\ &w_a(r_a, z_a) = -2b^{1/3}\upsilon_f^{2/3} G(\xi), \end{aligned} \tag{8}$$

where primes denote the differentiation w.r.t ξ and the last term of Eq. (8) leads to yield:

$$w_A = -2b^{1/3}\upsilon_f^{2/3} f_w. \tag{9}$$

Here, $f_w = G(0)$ divulges the transparent mass flux dimensionless constraint with $f_w > 0$ and $f_w < 0$ resemble to blowing and suction, respectively, while $f_w = 0$ indicates the surface of the impermeable disk.

Now the similarity transformations are plugged into Eqs. (2) to (4), where Eq. (1) is identically satisfied and the rest of the equations are transformed to the following similarity ODEs:

$$\frac{\mu_{nf}/\mu_f}{\rho_{nf}/\rho_f} G''' + 2GG'' - G'^2 = 0, \tag{10}$$

$$\frac{1}{\Pr\left(\rho c_p\right)_{nf}/\left(\rho c_p\right)_f}\left(k_{nf}/k_f + \frac{4}{3}N_r\right) S'' + 2GS' = 0, \tag{11}$$

with boundary conditions:

$$\begin{cases} G(0) = f_w,\ G'(0) = \beta_A + \delta_A G''(0),\ S(0) = 1 + \delta_B S'(0) \\ G''(\xi) \to 2, S(\xi) \to 0 \text{ as } \xi \to \infty. \end{cases} \tag{12}$$

The dimensionless parameters in the aforesaid equations include the velocity slip parameter $\delta_A = (2 - \sigma_w/\sigma_w)\,\lambda_a \left(b/\upsilon_f\right)^{1/3}$, the Prandtl number $\Pr = \upsilon_f/\alpha_f$, the thermal slip factor $\delta_B = (2 - \sigma_{TA}/\sigma_{TA})$ $(2\gamma_A/\gamma_A + 1)\,\lambda_a/\Pr\left(b/\upsilon_f\right)^{1/3}$ and the radiation parameter $N_r = \left(4\sigma^a T_\infty^3\right)/k^a k_f$.

The quantities of engineering practical importance are the friction factor C_{fr_a} in the radial direction and the Nusselt number Nu_{r_a}, which are given as:

$$C_{fr_a} = \frac{\mu_{nf}}{\rho_f {u_w}^2}\left(\frac{\partial u_a}{\partial z_a}\right)\Big|_{z_a=0},\ Nu_{r_a} = \frac{r_a}{k_f\left(T_w - T_\infty\right)}\left(-k_{nf}\left(\frac{\partial T_a}{\partial z_a}\right) + \left(q_r\right)_w\right)\Big|_{z_a=0}. \tag{13}$$

Using similarity transformations in the above Eq. (13), we get Eq. (14):

$$\mathrm{Re}_{r_a}^{1/2} C_{fr_a} = \frac{\mu_{nf}}{\mu_f} G''(0),\ \mathrm{Re}_{r_a}^{-1/2} Nu_{r_a} = -\left(\frac{k_{nf}}{k_f} + \frac{4}{3}N_r\right) S'(0). \tag{14}$$

where $\mathrm{Re}_{r_a} = \dfrac{u_w r_a}{\upsilon_f}$ corresponds to the local Reynolds number.

3 Temporal Stability Analysis

In this segment, we study the stability of the multiple (upper and lower) solutions as time evolves. Merkin [36] was the first researcher to introduce the analysis of this technique, later; it was followed by Weidman et al. [37]. For the measured working procedure, initially, we start from the new variables as follows:

$$u_a = b^{2/3}\upsilon_f^{1/3} r_a \frac{\partial G(\xi, \Sigma)}{\partial \xi},\ \xi = \left(b/\upsilon_f\right)^{1/3} z_a,\ S(\xi, \Sigma) = \frac{T_a - T_\infty}{T_w - T_\infty}, w_a = -2b^{1/3}\upsilon_f^{2/3} G(\xi, \Sigma). \tag{15}$$

where $\Sigma = b^{2/3}\upsilon_f^{1/3} t_a$ symbolizes the new dimensionless time. Further, executing the above Eq. (15) into the time-dependent or unsteady form of the requisite governing Eqs. (2) to (4), which can take place the form as:

$$\frac{\mu_{nf}/\mu_f}{\rho_{nf}/\rho_f}\frac{\partial^3 G}{\partial \xi^3}+2G\frac{\partial^2 G}{\partial \xi^2}-\left(\frac{\partial G}{\partial \xi}\right)^2-\frac{\partial^2 G}{\partial \xi \partial \Sigma}=0, \tag{16}$$

$$\frac{1}{\Pr\left(\rho c_p\right)_{nf}/\left(\rho c_p\right)_f}\left(k_{nf}/k_f+\frac{4}{3}N_r\right)\frac{\partial^2 S}{\partial \xi^2}+2G\frac{\partial S}{\partial \xi}-\frac{\partial S}{\partial \Sigma}=0, \tag{17}$$

subject to the appropriate BCs:

$$\begin{cases}\dfrac{\partial G(0,\Sigma)}{\partial \xi}=\beta_A+\delta_A\dfrac{\partial G(0,\Sigma)}{\partial \xi^2},\ G(0,\Sigma)=f_w,\ S(0,\Sigma)=1+\delta_B\dfrac{\partial S(0,\Sigma)}{\partial \xi}\\ \dfrac{\partial^2 G(\xi,\Sigma)}{\partial \xi^2}\to 2, S(\xi,\Sigma)\to 0\ as\ \xi\to\infty.\end{cases} \tag{18}$$

According to Weidman et al. [37], the time-independent outcome $G = G_0$ and $S = S_0$ of the similarity Eqs. (10) to (12) are perturbed as follows:

$$G(\xi,\Sigma)=G_0(\xi)+e^{-\Gamma\Sigma}g(\xi),\ S(\xi,\Sigma)=S_0(\xi)+e^{-\Gamma\Sigma}s(\xi), \tag{19}$$

where the functions $g(\xi)$ and $s(\xi)$ in Eq. (19) are relatively small compared to $G_0(\xi)$ and $S_0(\xi)$. The stability of the outcomes is determined by the sign (positive or negative) of the eigenvalue Γ. Therefore, exercising Eq. (19) into the above Eqs. (16) and (17) which can take place the form as:

$$\frac{\mu_{nf}/\mu_f}{\rho_{nf}/\rho_f}g'''+2\left(G_0g''+G_0''g-G_0'g'\right)+\Gamma g'=0, \tag{20}$$

$$\frac{1}{\Pr\left(\rho c_p\right)_{nf}/\left(\rho c_p\right)_f}\left(k_{nf}/k_f+\frac{4}{3}N_r\right)s''+2\left(G_0s'+S_0'g\right)+\Gamma s=0, \tag{21}$$

along with BCs:

$$\begin{aligned}&g(0)=0, g'(0)=\delta_A g''(0),\ s(0)=\delta_B s'(0)\\ &g''(\xi)\to 0,\ s(\xi)\to 0\ as\ \xi\to\infty.\end{aligned} \tag{22}$$

The corresponding positive or negative values of Γ in the above Eqs. (20) and (21) are found by setting the value of $g''(0)$ or $s'(0)$. Without loss of generality, we set $g''(0) = 2$ and solve the set of coupled Eqs. (20) to (22) to find the eigenvalues Γ.

4 Numerical Technique

The set of similarity Eqs. (10) and (11) with appropriate BCs (12) were cracked computationally by employing the bvp4c package available in MATLAB. The working procedure of the considered bvp4c scheme is described in detail by Shampine et al. [38] as well as Khan et al. [39]. The recognized bvp4c approach was also built on a well-known finite difference approach that used the Lobatto IIIA collocation formula to construct a C^1-continuous result. The syntax of the bvp4c solver is demarcated by "Sol = bvp4c (@OdeBVP, @OdeBC, Solinit, Options)". Moreover, to start working on the employed technique, the system of second and third order equations is changed to the required first order by introducing the latest notations and rewriting them as follows:

$$G=Z_1, G'=Z_2, G''=Z_3, S=Z_4, S'=Z_5. \tag{23}$$

Now to utilize the aforementioned Eq. (23) in the dimensionless set of Eqs. (10)–(12) to derive the set of first-order ODEs, which has the form:

$$\frac{d}{d\xi}\begin{pmatrix} Z_1 \\ Z_2 \\ Z_3 \\ Z_4 \\ Z_5 \end{pmatrix} = \begin{pmatrix} Z_2 \\ Z_3 \\ \dfrac{\rho_{nf}/\rho_f}{\mu_{nf}/\mu_f}\left(Z_2^2 - 2Z_1Z_3\right) \\ Z_5 \\ -2\dfrac{\Pr\left(\rho c_p\right)_{nf}/\left(\rho c_p\right)_f}{\left(k_{nf}/k_f + (4N_r/3)\right)}Z_1Z_5 \end{pmatrix}. \tag{24}$$

To treat the above set of differential equations as an initial boundary value problem, the following unknown and known initial conditions are considered:

$$Z_1(0) = f_w, Z_2(0) = \beta_A + \delta_A Z_3(0), Z_3(0) = B_1, Z_4(0) = 1 + \delta_B Z_5(0), Z_5(0) = B_2. \tag{25}$$

Moreover, the above-mentioned constants B_1 and B_2 are guessed during the bvp4c numerical execution by utilizing an operational shooting algorithm as explained practically by Khan et al. [39], in such a way that the executed iterative process is repeated multiply until satisfying all the following boundary conditions at once:

$$Z_3(\xi) \to 2, Z_4(\xi) \to 0 \text{ as } \xi \to \infty. \tag{26}$$

Two alternative initial guesses for the values of the skin friction coefficient and the heat transfer rate are used to investigate the double (upper and lower) solutions. To get the preferred outcomes, the suitable starting estimate and thickness of the boundary layer ξ_∞ must be selected based on the parameters implemented. To authenticate the considered numerical scheme, the values of $G''(0)$ are compared with the case that has been reported in Weidman [30] for regular (viscous) fluid ($\varphi = 0$) with several values of β_A when $f_w = 0$ and $\delta_A = 0$ as presented in Table 2, which displays a satisfactory agreement. From this comparison, it can be noticed that the existing results for upper and lower branch solutions are usable and consistent. Therefore, we can conclude that the generated algorithm for the numerically investigating Agrawal (Cu-water) nanofluid flow can be used with great confident.

Table 2: A comparison of the $G''(0)$ with Weidman et al. [30] for different values of β_A when $\varphi = f_w = 0$ and $\delta_A = 0$

β_A	Weidman et al. [30]		Present results	
	Upper solution	Lower solution	Upper solution	Lower solution
0.0	2.0000	–	2.000000	–
−0.1	–	–	1.989232	−0.740443
−0.3	–	–	1.889508	−0.243924
−0.3304	1.8627	0.0000	1.862651	0.000000
−0.5	–	–	1.623120	0.131034

(Continued)

Table 2 (continued)

β_A	Weidman et al. [30]		Present results	
	Upper solution	Lower solution	Upper solution	Lower solution
−0.65	–	–	1.036491	0.695894
−0.6570	0.8825	0.8494	0.887479	0.842643

5 Analysis of Results and Discussion

The present work aims to investigate the influence of the distinguished parameters such as the moving disk parameter β_A, the velocity slip parameter δ_A, the thermal slip parameter δ_B, the radiation parameter N_r, the mass suction parameter f_w, and the nanoparticles volume fraction φ on the reduced heat transfer, temperature profile and reduced shear stress of the (Cu-water) nanofluid for the double results as revealed in Figs. 2 to 9. Moreover, the computational values of the reduced shear stress and heat transfer of the (Cu-water) nanofluid for the upper branch solution (UBS) and lower branch solution (LBS) with the influence of the several influential parameters when $\lambda = -1.5$ (shrinking sheet) and $\mathrm{Pr} = 6.2$ are elucidated in Tables 3 and 4, respectively. The numerical and graphical behavior of the eigenvalues Γ for several values of β_A is presented in Table 5 and Fig. 10, respectively. For the aims of computation, the fix values of the embedded distinguished factors are written as follows: $\beta_A = -1.4$, $f_w = 0.5$, $\delta_A = 0.05$, $\delta_B = 0.5$, $N_r = 1.5$ and $\varphi = 0.03$. Therefore, the UBS and LBS throughout the graphs are signified by the black solid and dash lines, respectively, while the small solid red, blue, and grey balls are called the bifurcation point. The stable solutions are found on the UB, while unstable solutions are found on the LB. The stable solutions are of physical interest because they may be tested experimentally or understood practically.

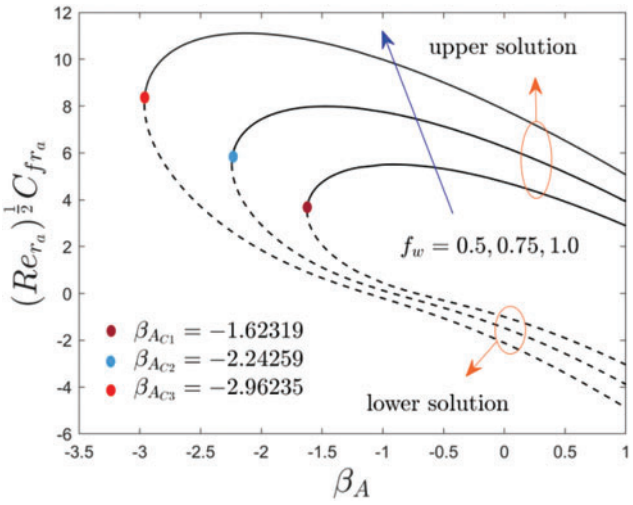

Figure 2: Variations of $\mathrm{Re}_{ra}^{1/2} C_{fr_a}$ against β_A for dissimilar choices of f_w

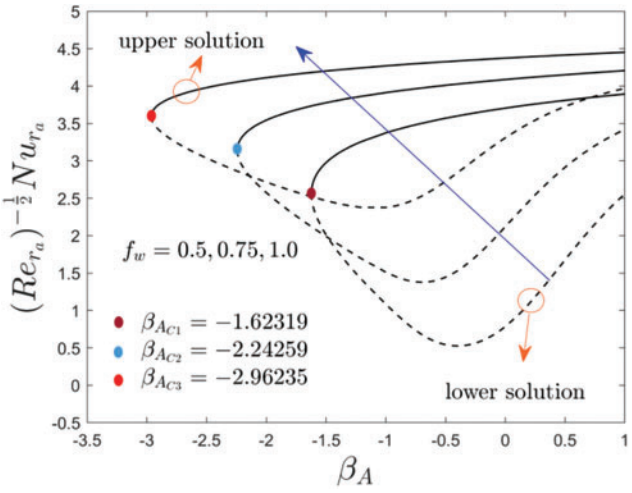

Figure 3: Deviations of $\mathrm{Re}_{r_a}^{-1/2} Nu_{r_a}$ against β_A for several values of f_w

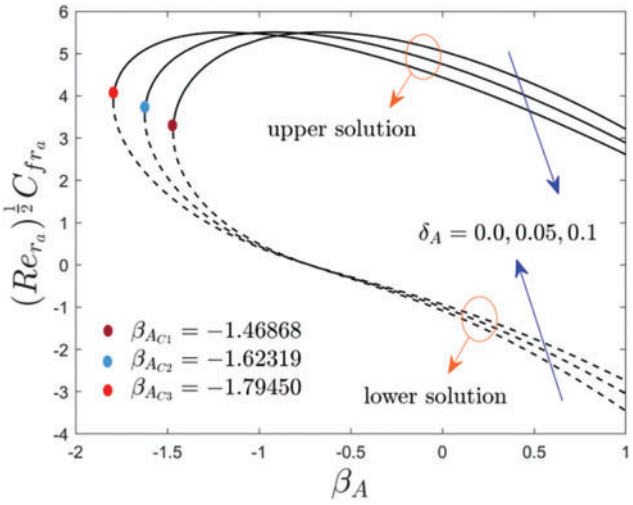

Figure 4: Variations of $\mathrm{Re}_{r_a}^{1/2} C_{fr_a}$ against β_A for dissimilar choices of δ_A

Table 3 displays the numerical values of the shear stress for the UB and LB outcomes with the influence of φ, f_w and δ_A when $\beta_A = -1.5$. From the table, it can be seen that the wall drag force upsurges for UB but decreases for the LB with higher values of f_w and δ_A while it is improved in two dissimilar branch results for developed impressions of φ. In addition, the wall drag force is higher for the stable result and lesser for the unstable outcome with f_w as compared to the consequence of the factors δ_A and φ. Alternatively, the numerical values of the heat transfer for the UB and LB results with the impact of φ, f_w, δ_A, N_r and δ_B when $\beta_A = -1.5$ and $\mathrm{Pr} = 6.2$ as highlighted in Table 4. The heat transport phenomenon elevates for UB as well as for LB with the higher impact of f_w, N_r and φ while it is shrinkages for UB and LB due to δ_B. Also, the impressions of δ_A can boost up the tendency of thermal transport for the stable result but decline for the unstable solution.

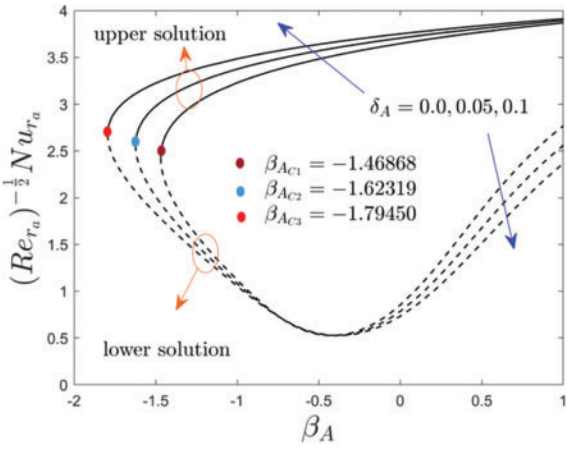

Figure 5: Variations of $\mathrm{Re}_{r_a}^{-1/2} Nu_{r_a}$ against β_A for several values of δ_A

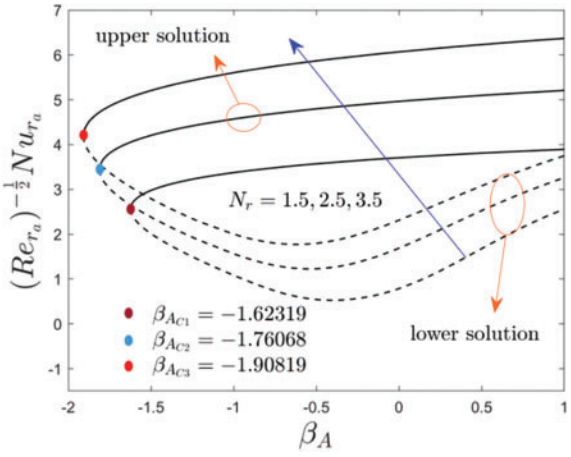

Figure 6: Variations of $\mathrm{Re}_{r_a}^{-1/2} Nu_{r_a}$ against β_A for dissimilar choices of N_r

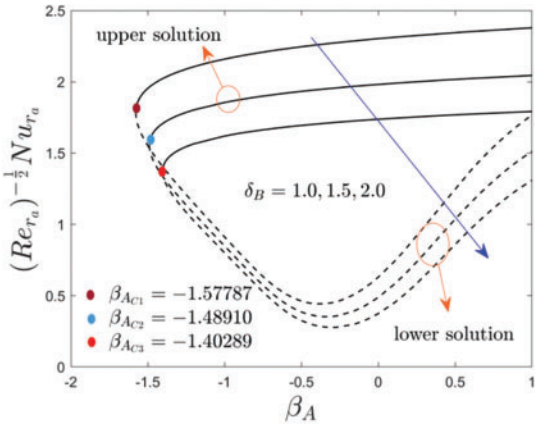

Figure 7: Deviations of $\mathrm{Re}_{r_a}^{-1/2} Nu_{r_a}$ against β_A for several values of δ_B

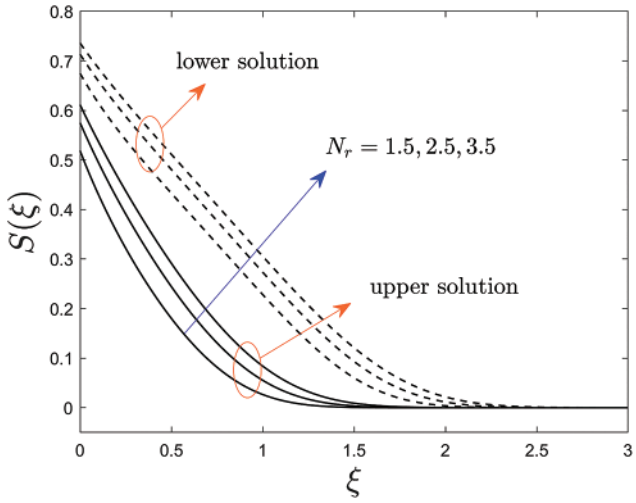

Figure 8: Variations of $S(\xi)$ against ξ for several values of N_r

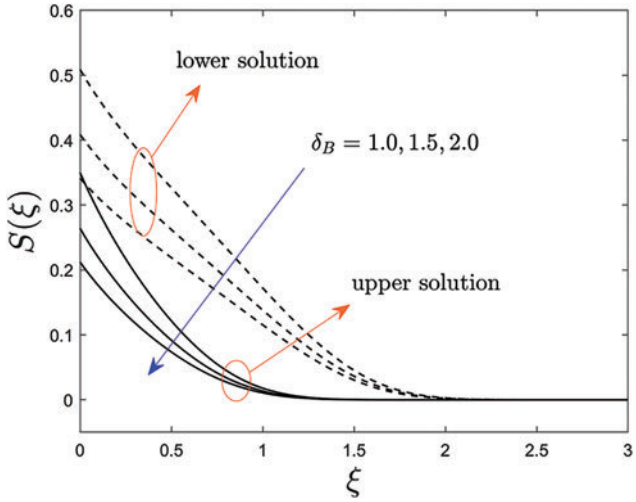

Figure 9: Variations of $S(\xi)$ against ξ for several values of δ_B

Table 3: Values of the wall drag force for the numerous distinct selected values of the parameters when $\beta_A = -1.5$ (shrinking sheet)

φ	f_w	δ_A	$\frac{\mu_{nf}}{\mu_f} G''(0)$	
			Upper solution	Lower solution
0.0	0.5	0.05	3.9173353	1.9102407
0.025			4.6086899	2.0437157
0.030			4.7466500	2.0714073

(Continued)

Table 3 (continued)

φ	f_w	δ_A	$\frac{\mu_{nf}}{\mu_f} G''(0)$	
			Upper solution	Lower solution
0.035			4.8845533	2.0994871
0.030	0.5	0.05	4.7466500	2.0714073
	0.75		7.9890041	1.1077096
	1.0		10.714728	0.6586701
	1.25		13.327741	0.2772573
0.030	0.5	0.0	4.1735618	2.0391455
		0.005	4.3009466	1.9695600
		0.05	4.7466500	2.0714073
		0.1	5.4264497	1.3348166

Table 4: Values of $-\left(k_{nf}/k_f + (4N_r)/3\right) S'(0)$ for the numerous values of the selected parameters when $\beta_A = -1.5$ (shrinking sheet) and $\Pr = 6.2$

φ	f_w	δ_A	N_r	δ_B	$-\left(\frac{k_{nf}}{k_f} + \frac{4}{3}N_r\right) S'(0)$	
					Upper solution	Lower solution
0.0	0.5	0.05	1.5	0.5	2.8339376	1.9697410
0.025					2.9558031	2.0051707
0.030					2.9776650	2.0119979
0.035					2.9988669	2.0187792
0.030	0.5	0.05	1.5	0.5	2.9776650	1.9697410
	0.75				3.7776385	2.0100598
	1.0				4.2014099	2.4684935
	1.25				4.4877776	3.1817618
0.030	0.5	0.0	1.5	0.5	2.7789586	1.9980300
		0.005			2.8219925	1.9675202
		0.05			2.9776650	1.8576342
		0.1			3.2932910	1.6598260
0.030	0.5	0.05	1.0	0.05	2.5449088	1.7387065
			1.5		2.9776650	2.0119979

(Continued)

Table 4 (continued)

φ	f_w	δ_A	N_r	δ_B	$-\left(\frac{k_{nf}}{k_f}+\frac{4}{3}N_r\right)S'(0)$	
					Upper solution	Lower solution
			2.0		3.3802264	2.2779136
			2.5		3.7610571	2.5375688
0.030	0.5	0.05	1.5	0.0	5.7423731	2.9821474
				0.1	4.8430384	2.7198544
				0.5	2.9776650	2.0119979
				1.0	2.0099565	1.5181234

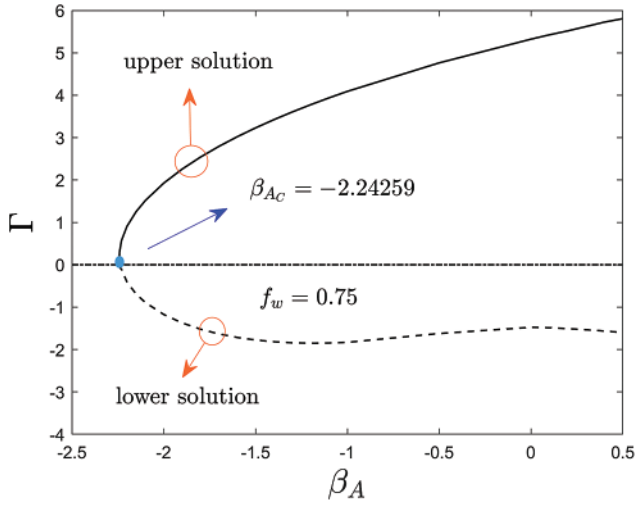

Figure 10: Eigenvalues of Γ for several values of β_A

Figs. 2 to 7 elucidate the variation of wall drag force $\mathrm{Re}_{ra}^{1/2}C_{fra}$, and heat transfer $\mathrm{Re}_{ra}^{-1/2}Nu_{ra}$ of the copper water-based nanofluid against β_A due to the influence of f_w, δ_A, N_r and δ_B, respectively. From these figures, it can be seen that two distinct branch solutions exist for the Eqs. (10) to (12) in the range of $\beta_A > \beta_{A_C}$ for both moving disk parameter or stretching/shrinking parameter, a unique solution found when $\beta_A = \beta_{A_C}$ and no solution is obtained when $\beta_A < \beta_{A_C}$, whereas, β_{A_C} corresponds the bifurcation value of β_A which the upper and lower solution merge.

Moreover, Figs. 2 and 3 show the inspirations of f_w on the wall friction force and heat transfer of the (Cu-water) nanofluid against β_A. From the responses, it is observed that the upswing of f_w augments the wall drag force for the UBS but declines for the LBS while $-\left(k_{nf}/k_f + (4N_r)/3\right)S'(0)$ is expressively widened with both (UB and LB) solutions. The existence of the solution domain for the occurrence of multiple (UB and LB) solutions is also increasing with the developed impressions of f_w. Physically, an increase in f_w causes a flow of nanoparticles towards the moving disk surface, as a result, lowering the velocity, and hence the wall drag coefficient is developing. Therefore, the gap between the UB curves is relatively more as compared to the curves of the LB (see Figs. 2 and 3). For growing values of f_w the

magnitude of bifurcation values (BVs) get developed. Therefore, the following BVs are found such as -1.62319, -2.24259, and -2.96235 for the respective selected values of f_w. This trend recommends that growing values of f_w decelerates the separation of boundary layers.

In Figs. 4 and 5, the variations of the multiple (UB and LB) solutions with the change of the velocity slip parameter δ_A are demonstrated with the wall drag force and heat transfer of the copper water-based nanoparticles, respectively. For growing values of δ_A, the wall drag force decreases and increases for the UBS in the specific range of β_A while it is followed the contrary patterns for the LBS as compared to UBS for higher δ_A. Physically, the liquid particles and the motion of the disk are different at the surface of the moving disk in the corresponding Maxwell slip BCs phenomena, which devalues the motion of fluid and specially the outcomes drop in the velocity fields. As a result, the friction factor in the radial path upsurges near the bifurcation point. In contrast, the heat transfer enriches for upper branch solution with larger values of δ_A while the impacts of δ_A is reversed for the lower solution curves. Moreover, the wall drag force behavior of the solution changes twice (for the UBS as well as for the LBS) at some finite value β_0 of β_A due to the larger value of δ_A while for heat transfer it is changed the only single time for the LBS curves. Owing to the improvement of the velocity slip parameter δ_A, the bifurcation values of the moving disk parameter are -1.46868, -1.62319, and -1.79450, respectively. In this respect, the separation of the boundary layer becomes suspended with the superior value of δ_A.

The influence of the radiation parameter N_r and temperature slip parameter δ_B on the heat transfer against β_A is revealed in Figs. 6 and 7, respectively. From the outcomes, it is perceived that the rate of heat transfer elevates for both solution branches with N_r but decelerates due to the larger value of δ_B. Generally, the liquid particles attract more thermal heat by increasing the radiation parameter; as a response, the heat transfer increases (see Fig. 6). In addition, with the selected change value of N_r, the subsequent BVs are found such as -1.62319, -1.76068, and -1.90819, respectively. To see more deeply, the pattern of the BVs decreases with N_r and consequently, the separation of boundary layer shrinkages. Alternatively, the magnitude of the BVs $|\beta_{A_C}|$ reduces for the larger value of δ_B as presented in Fig. 7. Therefore, the behavior of the solution curves specifies that the boundary layer separation augments with δ_B.

Figs. 8 and 9 describe the behavior of the typical temperature profiles for the multiple solutions of the copper-water base nanoparticles against the pseudo-similarity variable ξ with N_r and δ_B, respectively. The temperature profile in Fig. 8 augments for both branches of solution with a rise in N_r. The physical reason is that N_r is the key factor of the improvement of heat transfer. This situation is divulged that the $-\left(k_{nf}/k_f + (4N_r)/3\right) S'(0)$ enlarges via the asset of augmentation in the value of N_r. It is since an upsurge in N_r shrinkages the k^a which consequently drives to appreciation in temperature profiles. Conversely, the typical temperature decelerates for multiple (upper and lower) solutions due to the enhancement in the value of δ_B (see Fig. 9). The general reason is that the increment in δ_B lessening the distance between the wall moving surface of the disk and the free-stream temperature which convey less energy or heat to the liquid particles from the moving disk surface, and subsequently lessen the fluid temperature and the temperature profile as well.

Finally, Table 5 displays the eigenvalues Γ against β_A for the UB and LB solutions, while the rest of the comprised constraints are taken to be fixed. The data shown in the table are further plotted in the form of a graph (see Fig. 10) which can distinguish the behavior of the upper and lower solution noticeably. This graph is drawn for the positive and negative values of Γ against β_A. So, for the obtained smallest positive numerical values of Γ, it is distinguished that $e^{-\Gamma\Sigma} \to 0$ as time evolves ($\Sigma \to \infty$). In the meantime, for the negative numerical values of Γ, it is observed that $e^{-\Gamma\Sigma} \to 0$ as time evolves

($\Sigma \to \infty$). Therefore, the UBS is stable and hence physically trustworthy as $\Sigma \to \infty$, while the LBS is not.

Table 5: The numerical eigenvalues of Γ for several values of β_A

β_A	Upper solution	Lower solution
−2.24259	0.0	0.0
−2.24	0.3060	−0.0573
−2.23	0.5694	−0.1039
−2.2	0.9070	−0.4053
−2.15	1.2542	−0.6912
−2.1	1.5151	−0.8897
−2	1.9249	−1.1718
−1.9	2.2555	−1.3706
−1.8	2.5394	−1.5186
−1.7	2.7912	−1.6303
−1.6	3.0193	−1.7139
−1.5	3.2287	−1.7746
−1.4	3.4229	−1.8158
−1.3	3.6045	−1.8400
−1.2	3.7754	−1.8493
−1.1	3.9369	−1.8451
−1	4.0903	−1.8289
−0.5	4.7625	−1.6215
0	5.3221	−1.4749
0.1	5.4240	−1.4850
0.3	5.6196	−1.5324
0.5	5.8052	−1.5992

6 Conclusions

The influence of Maxwell velocity and Smoluchowski temperature slip conditions on the Agrawal steady axisymmetric SPF of (Cu-water) nanofluid via a moving continuous disk comprising the significant impacts of suction/injection owing to solar energy radiation has been examined. The employment of a similarity transformation for the steady Agrawal nanofluid flow is of particular relevance in this work. The significant outcomes are summarized as follows:

- The shear stress and heat transfer have been found to show double (UB and LB) solutions over a wide range of moving disk parameter or stretching/shrinking parameter.
- The shear stress uplifts due to f_w in the UB solution and shrinks in the case of LB solution; however, the heat transfer augments due to f_w in both cases.
- The heat transfer for the upper and lower solution branches enhances due to N_r, while it shrinkages with a higher value of δ_B.

- The thermal boundary layer thickness of (Cu-water) nanofluid is decayed for both branches owing to the development of δ_B, while it is strengthened due to the larger value of N_r.
- The domain of existence of multiple (upper and lower) solutions significantly improves for the larger values of the temperature slip parameter, radiation parameter, velocity slip parameter, and suction parameter.
- The velocity slip parameter δ_B has a dramatic impact on the shear stress for the UB and LB solutions while the heat transfer rate is increased and decreased significantly with a higher value of δ_B for the UB and LB solutions, respectively.
- The magnitude of the bifurcation or critical values enhances due to enlarging values of N_r, f_w and δ_B, but reduces with the superior value of δ_B.
- The boundary layer separation is delayed or broken down with a higher impact of N_r, f_w and δ_B while the separation of the boundary layer is escalated owing to a higher value of δ_B.
- Well-disposed to the analysis of stability, it was established that the UB solution is physically stable and trustworthy, while the LB solution is not.

The influence of nanoparticles on the absorption of radiative energy has been of interest for many years in a variety of applications. Nowadays, researchers are interested in the radiation properties of nanoparticles in liquid suspensions, especially for medical and other engineering or technical applications. In addition to the advantages of optical and radiative properties, nanofluids provide other advantages such as improved thermal conductivity and particle stability over micrometer-sized suspensions and the operation of direct-absorbing solar collectors. Nanofluids have been shown to possess improved heat transport properties and higher energy efficiency in a variety of thermal exchange systems for different industrial applications, such as transportation, electronic cooling, military, nuclear energy, aerospace, etc. Nanofluids powered by solar energy are important because they can be used in many heat transfers and other applications such as detergents, solar panels, drying processes, heat exchangers, geothermal and oil recovery, and building construction, etc.

7 Future Work

The future potential investigations of interest are as follows:

- The current work can be extended by considering the hybrid nanofluids to investigate the Agrawal flow.
- The time-dependent flow may be considered in future work.
- The mixed convection flow may be considered.

Acknowledgement: This research was supported by Researchers Supporting Project No. (RSP-2021/33), King Saud University, Riyadh, Saudi Arabia.

Funding Statement: The authors received the financial support from King Saud University, Riyadh, Saudi Arabia through Project No. RSP-2021/33.

Conflicts of Interest: The authors declare that they have no conflicts of interest to report regarding the present study.

References

1. Angstrom, A. K. (1924). Solar and terrestrial radiation. *Quarterly Journal of the Royal Meteorological Society, 50(210),* 121–126. DOI 10.1002/qj.49705021008.
2. Keshavarz, M. M., Majid, H. (2012). Modeling of turbulent forced convective heat transfer and friction factor in a tube for Fe_3O_4 magnetic nanofluid with computational fluid dynamics. *International Communications in Heat and Mass Transfer, 39(8),* 1293–1296. DOI 10.1016/j.icheatmasstransfer.2012.07.003.
3. Hunt, A. J. (1978). Small particle heat exchangers. *Journal of Renewable and Sustainable Energy*. Lawrence Berkeley Laboratory Report No. LBL-7841.
4. Lu, L., Liu, Z. H., Xiao, H. S. (2011). Thermal performance of an open thermosyphon using nanofluids for high-temperature evacuated tubular solar collectors: Part 1: Indoor experiment. *Solar Energy, 85(2),* 379–387. DOI 10.1016/j.solener.2010.11.008.
5. Kandasamy, R., Muhaimin, I., Khamis, A. B., Roslan, R. B. (2013). Unsteady Hiemenz flow of Cu-nanofluid over a porous wedge in the presence of thermal stratification due to solar energy radiation: Lie group transformation. *International Journal of Thermal Sciences, 65,* 196–205. DOI 10.1016/j.ijthermalsci.2012.10.013.
6. Anbuchezhian, N., Srinivasan, K., Chandrasekaran, K., Kandasamy, R. (2013). Magneto-hydrodynamic effects on natural convection flow of a nanofluid in the presence of heat source due to solar energy. *Meccanica, 48(2),* 307–321. DOI 10.1007/s11012-012-9602-x.
7. Kandasamy, R., Muhaimin, I., Rosmila, A. K. (2014). The performance evaluation of unsteady MHD non-Darcy nanofluid flow over a porous wedge due to renewable (solar) energy. *Renewable Energy, 64,* 1–9. DOI 10.1016/j.renene.2013.10.019.
8. Eid, M. R., Makinde, O. D. (2018). Solar radiation effect on a magneto nanofluid flow in a porous medium with chemically reactive species. *International Journal of Chemical Reactor Engineering, 16(9),* 20170212. DOI 10.1515/ijcre-2017-0212.
9. Talebi, M. H., Kalantar, V., Nazari, M. R., Kargarsharifabad, H. (2019). Experimental investigation of the forced convective heat transfer of hybrid Cu/Fe_3O_4 nanofluids. *Journal of Solid and Fluid Mechanics, 8(4),* 229–238. DOI 10.22044/JSFM.2019.7350.2687.
10. Acharya, N. (2020). On the flow patterns and thermal behaviour of hybrid nanofluid flow inside a microchannel in presence of radiative solar energy. *Journal of Thermal Analysis and Calorimetry, 141(4),* 1425–1442. DOI 10.1007/s10973-019-09111-w.
11. Asadikia, A., Mirjalily, S. A. A., Nasirizadeh, N., Kargarsharifabad, H. (2020). Hybrid nanofluid based on CuO nanoparticles and single-walled Carbon nanotubes: Optimization, thermal, and electrical properties. *International Journal of Nano Dimension, 11(3),* 277–289. DOI 20.1001.1.20088868.2020.11.3.8.0.
12. Asadikia, A., Mirjalily, S. A. A., Nasirizadeh, N., Kargarsharifabad, H. (2020). Characterization of thermal and electrical properties of hybrid nanofluids prepared with multi-walled carbon nanotubes and Fe_2O_3 nanoparticles. *International Communications in Heat and Mass Transfer, 117(4),* 104603. DOI 10.1016/j.icheatmasstransfer.2020.104603.
13. Sarkar, A., Kundu, P. K. (2021). Framing the upshot of Hall current on MHD unsteady nanofluid flow from a rotating spherical body in presence of solar radiation. *International Journal of Ambient Energy,* 1–11. DOI 10.1080/01430750.2021.1965021.
14. Asadikia, A., Mirjalily, S. A. A., Nasirizadeh, N., Kargarsharifabad, H. (2021). Experimental study of thermal conductivity of water/ethylene glycol-Fe_2O_3/SWNCT composite nanofluid and its optimization using neural networks and genetic algorithms. *Journal of Nanomaterials, 13(45),* 1–14. DOI 20.1001.1.20086156.1400.13.45.1.3.
15. Chamkha, A. J., Armaghani, T., Mansour, M. A., Rashad, A. M., Kargarsharifabad, H. (2021). MHD convection of an Al_2O_3 Cu/water hybrid nanofluid in an inclined porous cavity with internal heat generation/absorption. *Iranian Journal of Chemistry and Chemical Engineering, 1,* 1–10. DOI 10.30492/IJCCE.2021.136201.4328.

16. Shoeibi, S., Kargarsharifabad, H., Rahbar, N., Ahmadi, G., Safaei, M. R. (2022). Performance evaluation of a solar still using hybrid nanofluid glass cooling-CFD simulation and environmental analysis. *Sustainable Energy Technologies and Assessments, 49(4),* 101728. DOI 10.1016/j.seta.2021.101728.
17. Navier, C. L. M. H. (1827). Mémoire sur les lois du mouvement des fluids. *Mémoires de l'Académie des Sciences, 6,* 389–391.
18. Maxwell, J. C. (1878). On stresses in rarefied gases arising from inequalities of temperature. *Proceedings of the Royal Society of London, 27(185–189),* 304–308. DOI 10.1098/rspl.1878.0052.
19. Smoluchowski, M. V. (1898). Ueber Wärmeleitung in verdünnten Gasen. *Annalen der Physik, 300(1),* 101–130. DOI 10.1002/(ISSN)1521-3889.
20. Ramya, D., Raju, R. S., Anand, J. A., Chamkha, A. J. (2018). Effects of velocity and thermal wall slip on magnetohydrodynamics (MHD) boundary layer viscous flow and heat transfer of a nanofluid over a non-linearly-stretching sheet: A numerical study. *Propulsion and Power Research, 7(2),* 182–195. DOI 10.1016/j.jppr.2018.04.003.
21. Khashi, N. S., Arifin, N. M., Pop, I., Nazar, R., Hafidzuddin, E. H. et al. (2020). Three-dimensional hybrid nanofluid flow and heat transfer past a permeable stretching/shrinking sheet with velocity slip and convective condition. *Chinese Journal of Physics, 66(4),* 157–171. DOI 10.1016/j.cjph.2020.03.032.
22. Jünemann, T., Pleskun, H., Brümmer, A. (2021). Maxwell velocity slip and Smoluchowski temperature jump boundary condition for ANSYS CFX. *IOP Conference Series: Materials Science and Engineering, 1180(1),* 012037. DOI 10.1088/1757-899X/1180/1/012037.
23. Sajid, T., Jamshed, W., Shahzad, F., Akgül, E. K., Nisar, K. S. et al. (2022). Impact of gold nanoparticles along with Maxwell velocity and Smoluchowski temperature slip boundary conditions on fluid flow: Sutterby model. *Chinese Journal of Physics, 77(2),* 1387–1404. DOI 10.1016/j.cjph.2021.11.011.
24. Hiemenz, K. (1911). Die Grenzschicht an einem in den gleichformingen Flussigkeitsstrom eingetauchten graden Kreiszylinder. *Dinglers Polytechnisches Journal, 326,* 321–324.
25. Homann, F. (1936). Der Einfluss grosser Zahigkeit bei der Stromung um den Zylinder und um die Kugel. *Journal of Applied Mathematics and Mechanics, 16(3),* 153–164. DOI 10.1002/zamm.19360160304.
26. Howarth, L. (1951). The boundary layer in three dimensional flow–Part II, the flow near a stagnation point. *Philosophical Magazine and Journal of Science, 42(335),* 1433–1440. DOI 10.1080/14786445108560962.
27. Davey, A. (1961). Boundary layer flow at a saddle point of attachment. *Journal of Fluid Mechanics, 10(4),* 593–610. DOI 10.1017/S0022112061000391.
28. Agrawal, H. L. (1957). A new exact solution of the equations of viscous motion with axial symmetry. *The Quarterly Journal of Mechanics and Applied Mathematics, 10(1),* 42–44. DOI 10.1093/qjmam/10.1.42.
29. Weidman, P. (2015). Axisymmetric rotational stagnation-point flow impinging on a rotating disk. *Zeitschrift für Angewandte Mathematik und Physics, 66(6),* 3425–3431. DOI 10.1007/s00033-015-0587-x.
30. Weidman, P. (2016). Axisymmetric rotational stagnation point flow impinging on a flat liquid surface. *European Journal of Mechanics-B/Fluids, 56,* 188–191. DOI 10.1016/j.euromechflu.2015.11.012.
31. Weidman, P. (2016). Axisymmetric rotational stagnation point flow impinging on a radially stretching sheet. *International Journal of Non-Linear Mechanics, 82,* 1–5. DOI 10.1016/j.ijnonlinmec.2016.01.016.
32. Roşca, N. C., Pop, I. (2017). Axisymmetric rotational stagnation point flow impinging radially a permeable stretching/shrinking surface in a nanofluid using Tiwari and Das model. *Scientific Reports, 7(1),* 40299. DOI 10.1038/srep40299.
33. Fathalah, K. A., Elsayed, M. M. (1980). Natural convection due to solar radiation over a non-absorbing plate with and without heat losses. *International Journal of Heat and Fluid Flow, 2(1),* 41–45. DOI 10.1016/0142-727X(80)90007-7.
34. Acharya, N., Das, K., Kundu, P. K. (2016). The squeezing flow of Cu-water and Cu-kerosene nanofluids between two parallel plates. *Alexandria Engineering Journal, 55(2),* 1177–1186. DOI 10.1016/j.aej.2016.03.039.

35. Hayat, T., Qayyum, S., Khan, M. I., Alsaedi, A. (2018). Entropy generation in magnetohydrodynamic radiative flow due to rotating disk in presence of viscous dissipation and Joule heating. *Physics of Fluids, 30(1),* 017101. DOI 10.1063/1.5009611.

36. Merkin, J. H. (1986). On dual solutions occurring in mixed convection in a porous medium. *Journal of Engineering Mathematics, 20(2),* 171–179. DOI 10.1007/BF00042775.

37. Weidman, P. D., Kubitschek, D. G., Davis, A. M. J. (2006). The effect of transpiration on self-similar boundary layer flow over moving surfaces. *International Journal of Engineering Science, 44(11–12),* 730–737. DOI 10.1016/j.ijengsci.2006.04.005.

38. Shampine, L. F., Thompson, S. (2001). Solving DDEs in MATLAB. *Applied Numerical Mathematics, 37(4),* 441–458. DOI 10.1016/S0168-9274(00)00055-6.

39. Khan, U., Waini, I., Ishak, A., Pop, I. (2021). Unsteady hybrid nanofluid flow over a radially permeable shrinking/stretching surface. *Journal of Molecular Liquids, 331(3),* 115752. DOI 10.1016/j.molliq.2021.115752.